Flow in deformable porous media. Part 2 Numerical analysis – the relationship between shock waves and solitary waves

By MARC SPIEGELMAN

Lamont-Doherty Geological Observatory of Columbia University, Palisades, NY 10964, USA

Using numerical schemes, this paper demonstrates how viscous resistance to volume changes modifies the simplest shock wave solutions presented in Part 1. For an initial condition chosen to form a step-function shock, viscous resistance causes the shock to disperse into a rank-ordered wavetrain of solitary waves. Large obstructions in flux produce large-amplitude, slow-moving wavetrains while smaller shocks shed small-amplitude waves. While the viscous resistance term is initially important over a narrow boundary layer, information about obstructions in the flux can propagate over many compaction lengths through the formation of non-zero wavelength porosity waves. For large-amplitude shocks, information can actually propagate backwards relative to the matrix. The physics of dispersion is discussed and a physical argument is presented to parameterize the amplitude of the wavetrain as a function of the amplitude of the predicted shock. This quantitative relationship between the prediction of shocks and the development of solitary waves also holds when mass transfer between solid and liquid is included. Melting causes solitary waves to decrease in amplitude but the process is reversible and freezing can cause small perturbations in the fluid flux to amplify into large-amplitude waves. These model problems show that the equations governing volume changes of the matrix are inherently time dependent. Perturbations to steady-state solutions propagate as nonlinear waves and these problems demonstrate several initial conditions that do not relax to steady state. If these equations describe processes such as magma migration in the Earth, then these processes should be inherently episodic in space and time.

1. Introduction

Simple analysis described in Part 1 (Spiegelman 1993) shows that the equations governing the volume changes of a viscously deformable permeable medium describe a nonlinear wave equation for the evolution of porosity. This analysis also shows that many simple initial conditions will develop porosity shock waves in the absence of viscous resistance of the matrix to volume changes. In the vicinity of a rapid change in the melt flux, however, viscous stresses in the matrix cannot be negligible. This paper continues the analysis using numerical methods and demonstrates that viscous resistance to volume changes causes simple shocks to disperse into trains of solitary waves.

To date there has been little success in obtaining analytic solutions to the full

nonlinear equations for non-steady-state initial conditions.† Because the solitary waves do not appear to be solitons (Barcilon & Richter 1986), it is not clear that an exact analytic method for general initial conditions, such as the inverse scattering transform, exists for these equations. Therefore, until adequate approximate techniques are developed, we must rely on accurate numerical methods.

The governing equations in potential form (Part 1, (18)–(20)) can be solved using standard numerical techniques. This paper uses finite-difference schemes for one- and two-dimensional problems. To maintain second-order accuracy and minimize numerical diffusion, we use a staggered leapfrog scheme to update the porosity via (18) of Part 1. Equation (19) is solved by tridiagonal elimination in one dimension and by alternating-direction-implicit (ADI) relaxation in two dimensions. These differencing schemes are described in detail in Press *et al.* (1986). The problems presented in this paper are solved using the small-ϕ_0 approximation (Part 1) in order to simplify the analysis of the characteristic solutions and the solitary waves. For porosities well below the limit where the solid matrix disaggregates ($\phi_0 \lesssim 20\%$), inclusion of the terms of order ϕ_0 does not change the criteria for shocks to form or modify the elliptic viscous resistance term. Barcilon & Richter (1986) compare the solutions for one-dimensional solitary waves in the full equations and in the small-ϕ_0 approximation. They show that the differences between the two solutions are negligible ($\sim 1\%$) for waves with maximum dimensional porosities less than 30%. In two dimensions, the ϕ_0 terms will cause matrix convection which can be included using standard Poisson and biharmonic solvers. For accuracy and resolution, however, this paper restricts quantitative solutions to one dimension.

The numerical schemes have been tested against the analytic solution for solitary waves with permeability exponent $n = 3$ in the limit that $\phi_0 \ll 1$ (Scott & Stevenson 1984; Barcilon & Richter 1986). Results of these tests are given in Appendix A and show that the numerical schemes can accurately resolve the solitary waves. The amplitude of well-resolved waves remains within 0.1% of the analytic value. Errors in phase velocity are less than 0.2% of the true value. These numerical errors are much smaller than any of the variations in amplitude or velocity seen in the numerical calculations.

2. A comparison between characteristic and numerical solutions: one dimension, no melting

The effect of viscous resistance to volume changes is readily explored by comparing numerical solutions of the full equations to analytic solutions of the zero-compaction-length approximation. The only difference between these two sets of equations is the elliptic term, $\nabla \cdot k_\phi \nabla \mathscr{C}$, in (18) of Part 1 (where k_ϕ is the permeability and $\mathscr{C}$ is the compaction rate). This section demonstrates qualitatively that the zero-compaction-length approximation is relatively accurate for problems where viscous resistance is transient. For initial conditions where shocks are predicted, however, viscous resistance to volume changes causes the shocks to disperse into a series of nonlinear solitary waves.

As an example of a problem where the zero-compaction-length approximation is valid, consider the compaction of a constant-porosity half-space onto an impermeable surface. This problem relaxes to a steady state without developing shocks, and has

---

† The major analytic success for these equations has been for waveforms of permanent form and constant phase velocity. Under these requirements, the equations can be transformed to steady state ODEs in the new variable $z' = z - ct$ and solved by standard techniques.
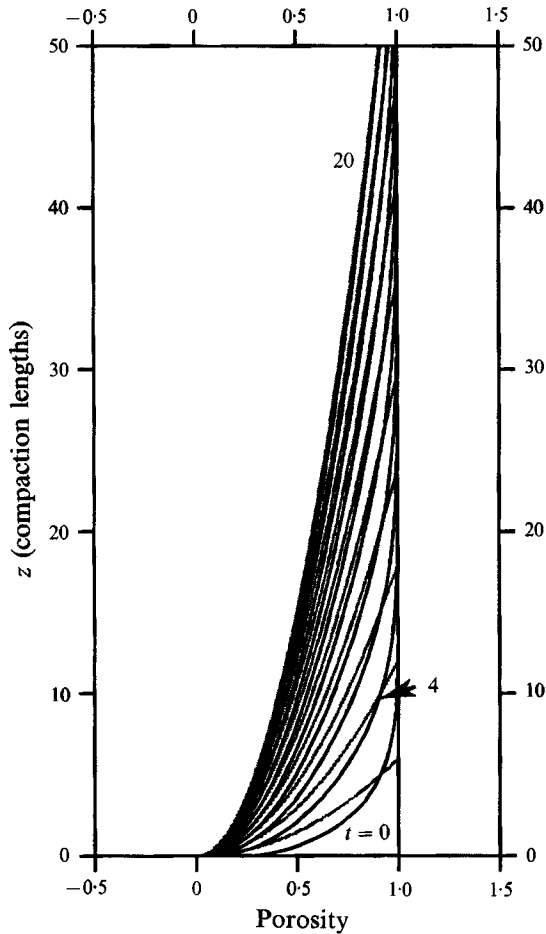
FIGURE 1. A comparison of full and approximate solutions for the time-dependent compaction of a constant-porosity layer onto an impermeable surface. Dimensionless porosity profiles are shown at time intervals of $t = 2$ (non-dimensional) to $t_{max} = 20$. Both solutions use a permeability exponent of $n = 3$, and assume $\phi_0 \ll 1$. Solid curves show the numerical solution of the full equations including viscous resistance to volume changes. Shaded curves show the analytic approximate solution given by the method of characteristics. For $t \gtrsim 10$ this solution is very close to the numerical solution. Both solutions relax smoothly towards steady state.

been discussed at length by McKenzie (1984). Numerical solutions are given by Richter & McKenzie (1984), and Richter (1986). In figure 1, a numerical solution of the full equations is compared to an analytic solution of the approximate equations for a layer that is 50 compaction lengths deep. For the analytic solution, the initial porosity distribution, $\phi_i(z)$, evolves along straight characteristics with phase velocity $v_\phi = 3\phi_i^2$. Thus, the position of the initial discontinuity with time is simply $3t$. For times greater than $t \sim 10$, the two solutions are nearly indistinguishable while at earlier times more significant differences are seen. In particular, the numerical solution, which includes viscous resistance, is retarded relative to the analytic solutions. This is because viscous resistance to volume changes will be most important where the gradient of the melt flux is large. The elliptic term affects the early evolution of porosity but becomes negligible with time. For a smoother initial porosity profile, the two solutions are nearly identical at all times.
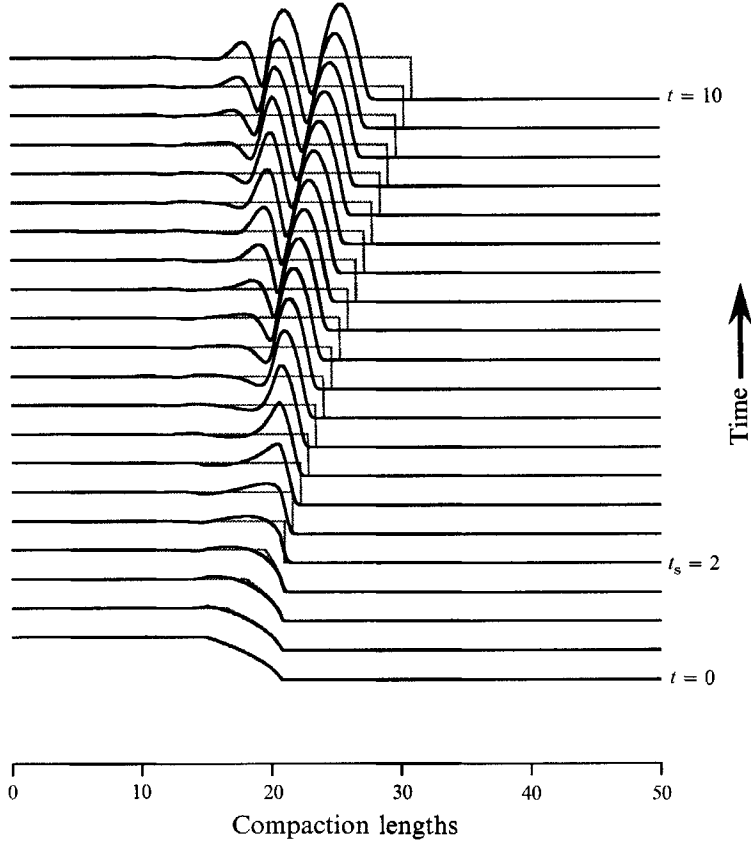
FIGURE 2. Characteristic and numerical solutions for the evolution of porosity from an initial condition that develops into a perfect step-function shock at time $t_s = 2$ in the zero-compaction-length approximation. The dotted lines show the analytic shock solution to the approximate equations. After $t = t_s$, this shock travels as a perfect step with $\phi_{max} = 1$, $\phi_1 = 0.2$ at constant velocity $c_s = 1.24$. The solid lines show the numerical solution to the full equations for the same initial condition. Until $t = t_s$ the full and approximate solutions are comparable. For $t \geqslant t_s$, viscous resistance causes the shock to disperse into a series of porosity maxima and minima. In this example, the leading porosity wave travels slower than c_s ($c \sim 0.8$) and each new wave forms further back relative to the matrix.

When shocks are predicted, however, the behaviour of the solution of the full equations is significantly different. An initial condition that develops into a simple shock is

$$\phi = \begin{cases} 1, & z < 0, \\ [1 - (z/\lambda)(1 - \phi_1^{n-1})]^{1/(n-1)}, & 0 < z < \lambda, \\ \phi_1, & z > \lambda. \end{cases} \tag{1}$$

In the absence of viscous resistance to volume changes, this initial condition develops a perfect step function at time $t_s = \lambda/[n(1 - \phi_i^{n-1})]$ as long as $n > 1$. This step has a maximum dimensionless porosity of $\phi = 1$, a minimum porosity $\phi = \phi_1$ and a constant phase velocity, $c_s = (1 - \phi_1^n)/(1 - \phi_1)$ (see Part 1, figure 4). Note, for all ϕ_1 between 0 and 1, the shock always travels faster than the fastest melt velocity even as $\phi_1 \to 0$.

Figure 2 shows the shock solution (shaded line) for $\phi_1 = 0.2$, $n = 3$, $t_s = 2$ ($\phi_0 \ll 1$). Because porosity remains constant on characteristics (if there is no melting), porosity

gradients may steepen but the maximum porosity cannot grow. Moreover, because the zero-δ approximation has no intrinsic lengthscale, the initial variation in the flux remains localized to a single shock. When viscous resistance of the matrix to volume changes is included, however, the behaviour of the solution is quite different. The solid line in figure 2 is the numerical solution for the evolution of the identical initial condition superposed on the shock solution. Up to the time of shock formation the two solutions are similar. However, when the flux varies on a lengthscale comparable to the compaction length, the forward progress of the shock is retarded and the excess flux accumulates in a local porosity maximum. Rather than growing into a single 'bow wave' however, the growth of the maximum produces a region where locally the flux increases in the direction of flow. This rapid increase in flux drains melt from the region immediately upstream, producing a local porosity minimum where $\phi < 1$. This new minimum becomes a second obstruction in the flux which initiates a second maximum and so on. The end result is that the simple shock disperses into a growing train of non-zero-wavelength porosity waves. In this case the wavetrain actually grows faster than the leading wave moves forward, causing information to propagate backwards relative to the matrix. This back-propagation of information becomes more pronounced in calculations that are carried out to greater times.

This comparison illustrates that the elliptic compaction term can cause porosity both to increase and decrease and allows information about variations in the melt flux to propagate away from the area of the initial obstruction in flux. Section 3.2 shows that this behaviour is consistent with the form of the governing equations. Before considering the physics of dispersion, however, it is useful to investigate the evolution of this simple initial condition more quantitatively. The next section shows that these porosity waves, when well formed, behave as the solitary waves described by several authors (Scott & Stevenson 1984; Richter & McKenzie 1984; Barcilon & Richter 1986). The next problem also shows that dispersive wavetrains form for all numerically resolvable initial conditions with a single jump in the melt flux. We then quantify the relationship between the size of the obstruction and the amplitude of the solitary waves that are produced.

3. Quantifying the relationship between shocks and solitary waves: one-dimensional step shocks, no melting

The initial condition for this problem

$$\phi(z, 0) = \begin{cases} 1, & z < z_0, \\ \phi_1 + (1 - \phi_1) \operatorname{sech}((z - z_0)/\lambda), & z > z_0, \end{cases} \tag{2}$$

is similar to (1) except that the initial step has been smoothed slightly ($\lambda = 2.5$) to minimize numerical artifacts encountered at long times that arise from discontinuous and piecewise-continuous initial conditions. Without viscous effects, this initial condition would also evolve into a travelling step function shock after a short adjustment period in which the shock coalesces. Note that for a fixed permeability exponent n and in the limit of small porosity, the properties of the shock are determined by a single parameter, the minimum porosity ϕ_1. The properties of the dispersive porosity waves must also be only a function of ϕ_1 as the term governing viscous resistance contributes no new adjustable parameters. Solutions were calculated for $\phi_1 = 0.1$–0.9 to a dimensionless time of $t = 80$, which is sufficient for well-developed wavetrains to form. The boundary conditions are constant porosity
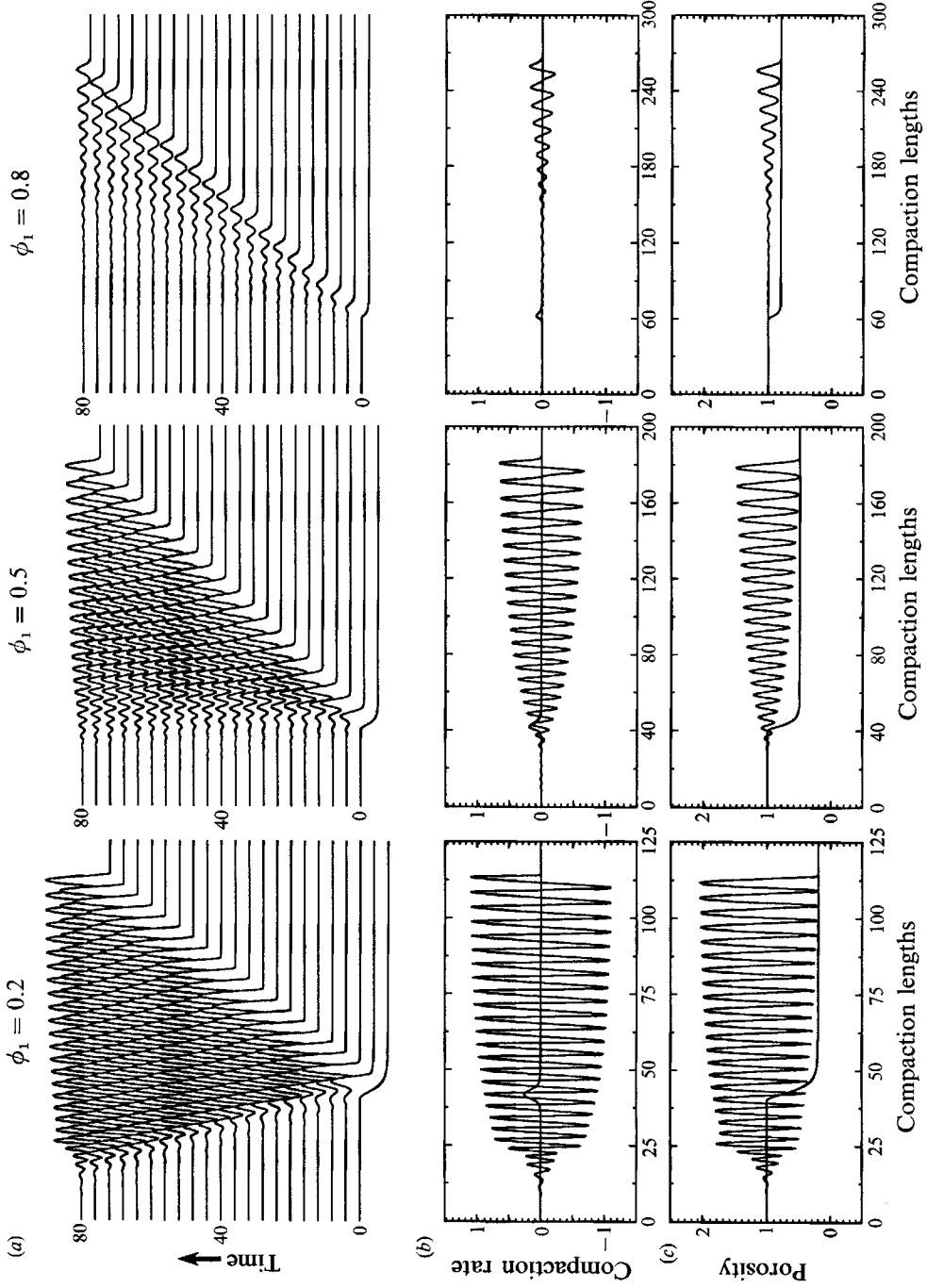
FIGURE 3. For caption see facing page.

(rigid) with $\phi(0) = 1$, $\phi(z_{max}) = \phi_1$ and $\mathscr{C}(0) = \mathscr{C}(z_{max}) = 0$. As long as the porosity waves remain at least a few compaction lengths away from the boundaries, this boundary condition reduces to a constant-flux boundary. The boundaries are deliberately placed far from the regions of rapid flux variation to avoid edge effects.

3.1. *Results*

Figure 3 shows porosity profiles as a function of time for minimum porosities $\phi_1 = 0.2, 0.5, 0.8$. Rather than developing into a discrete porosity front, this solution produces a rank-ordered, dispersive, wavetrain of porosity waves for all values of ϕ_1. While these waves are not 'solitary' (i.e. well separated), the best developed waves obey the same dispersion relationship as solitary waves of the same amplitude.

In more detail, figure 4 shows the distribution of amplitudes of the porosity maxima for each value of ϕ_1 at $t = 80$. Figure 4(*b*) shows the amplitude of the leading wave with time. At late times, the rank ordering of the wavetrain is clear with amplitudes of well-developed waves ranging between $\sim \pm 10$–20% of the mean value. The amplitude of the wavetrain is not constant; therefore, this solution is not the periodic wavetrain solution of Olson & Christensen (1986). Close examination of a series of conduit wave experiments by Scott & Stevenson (1986) that are similar to those of Olson & Christensen (1986) seem to show a definite rank ordering as well. The time dependence of the leading wave (figure 4*b*) is similar for all values of ϕ_1 and shows a rapid growth at early times followed by a long period of very slow growth. For the duration of the calculations shown here, the growth rate of the leading wave is always slightly positive. However, as the different waves move at different speeds (see below), the leading wave may stop growing if it separates from the rest of the wavetrain.

In addition to the amplitude, the phase velocity of these waves is time dependent. For well-developed waves, however, the instantaneous velocity of the porosity maximum approaches that of the solitary wave with amplitude $A(t)$. Figure 5(*a*) shows the phase velocity of the leading wave as a function of time. Each cross is the measured velocity of the porosity maximum calculated by the centred difference

$$\bar{c}(t) = \frac{z_p(t + \Delta t) - z_p(t - \Delta t)}{2\Delta t}, \tag{3}$$

where z_p is the position of the leading wave crest and $\Delta t = 2$ is the sampling time. For each value of ϕ_1, the continuous curve shows the theoretical phase velocity for the solitary wave of amplitude $A(t)$ with permeability exponent $n = 3$ and $\phi_0 \ll 1$. The dispersion relationship for these waves is given in Scott & Stevenson (1984) and Barcilon & Richter (1986); however, in these papers it is convenient to scale the

---

FIGURE 3. Evolution of a single smoothed step in porosity ($n = 3$, $\phi_0 \ll 1$). In the absence of viscous dispersion, this initial condition, (2), evolves to a travelling step-function shock with maximum porosity $\phi_{max} = 1$ and minimum porosity $\phi_{min} = \phi_1$. Viscous resistance to volume changes, however, causes the step to disperse into a rank-ordered dispersive wavetrain of solitary waves. For each value of ϕ_1, (*a*) shows porosity profiles *vs.* time for $t = 0$–80; (*b*) and (*c*) show superposed initial ($t = 0$) and final ($t = 80$) profiles for compaction rate and porosity. All finite-difference grids have $4\phi_1^{-\frac{3}{2}}$ grid points/compaction length. The large-amplitude shock ($\phi_1 = 0.2$) develops into a large-amplitude, slow-moving, back-propagating wavetrain. The smaller obstruction ($\phi_1 = 0.5$) develops smaller-amplitude, faster wavetrains (note the difference in scales) with all new waves initiating near $z = 40$. The smallest obstruction ($\phi_1 = 0.8$) produces a small-amplitude, fast-moving, forward-propagating, wavetrain.
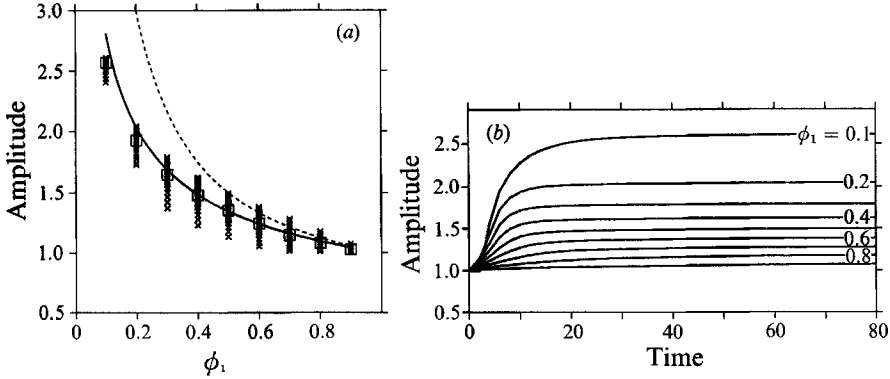
FIGURE 4. Amplitude variation of the dispersive wavetrain as a function of the minimum porosity ϕ_1. (a) Rank ordering of the wavetrains at $t = 80$. $\times$, the amplitude of the porosity maxima in the wavetrain; $\square$, the mean amplitude of the wavetrain. The dashed line is the amplitude of the solitary wave that travels at the same speed as the shock predicted in the zero-compaction-length approximation. For $\phi_1 < 0.5$, this argument significantly overestimates the amplitude of the wavetrain. The solid line is the relation for $A(\phi_1)$ as calculated by the physical argument of §3.3. (b) Amplitude of the leading wave as a function of time.
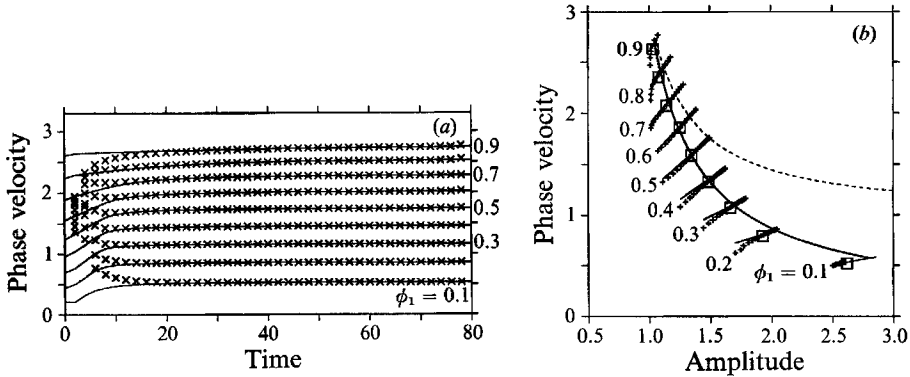

FIGURE 5. Variation of phase speed of the dispersive wavetrain as a function of ϕ_1 and amplitude. (a) Measured and theoretical phase speed of the leading porosity wave as a function of time: $\times$, the measured velocity of the leading wave at time t; the continuous line is the phase speed of the analytic solitary wave with the same amplitude $A(t)$. For dimensionless times $t \gtrsim 20$ the leading wave velocity is indistinguishable from the theoretical value. (b) Distribution of phase velocity and amplitude for all well-developed waves at $t = 78$: $+$, the measured phase speed and amplitude of each porosity maximum; the short, straight lines are the theoretical dispersion relations for solitary waves, $c(A, \phi_1)$; $\square$, the mean amplitude and phase speed of the wavetrain; the dashed curve shows the speed and amplitude of the solitary wave that travels at the speed of the predicted shock. For $\phi_1 < 0.5$, this argument grossly overestimates A and c for the wavetrain. The solid curve is the relation for $c(A(\phi_1))$ as calculated by the physical argument of §3.3.

porosity and velocity to the small background porosity. The dispersion relation corresponding to the scaling used here for the initial step in porosity is

$$c(A;\phi_1) = \phi_1^2(2A/\phi_1 + 1) = \phi_1(2A + \phi_1). \qquad (4)$$

Figure 5(a) shows that for all values of ϕ_1, and for times $t \gtrsim 20$, the phase velocity of the leading wave is indistinguishable from the theoretical phase velocity of the solitary wave. This match between the analytic and numerical phase velocities is a good indication that the waves are well resolved.

At late times, the leading wave behaves as a solitary wave of amplitude $A(t)$ moving over the uniform background porosity ϕ_1. This feature is also true of the other well-developed waves in the train. Figure 5(b) shows the measured phase velocity of porosity waves as a function of their amplitudes. Each plus sign marks the measured phase velocity calculated by (3) at $t = 78$. The short, straight line through the symbols is the dispersion relationship given by (4). Well-developed waves travel near the velocity of solitary waves while poorly developed waves travel more slowly than the solitary wave with the same amplitude.† Figure 5(b) also shows that this wavetrain is dispersive in the strict sense that each wave composing the train moves at a different velocity. Thus, there is no frame in which this solution appears to be in steady state. This result further demonstrates that this solution is not the periodic wavetrain of Olson & Christensen as their solution travels at constant phase velocity. It is not clear whether parts of the wavetrain would evolve towards a periodic solution at long times; however, the next section shows that there are no solutions of constant velocity and permanent form that satisfy the boundary conditions used here.

Perhaps the most important result of this model problem is the relationship between the properties of the wavetrain and the size of the jump in the melt flux (or the value of the minimum porosity ϕ_1). Large jumps in the initial flux develop into large-amplitude slow-moving wavetrains, while smaller obstructions produce smaller-amplitude fast-moving trains. This result is physically reasonable because a larger obstruction in the melt flux (smaller ϕ_1) causes more melt to accumulate in the leading waveform and makes it more difficult for the porosity to propagate into the region of small porosity. The next section shows that, in the limit that the obstruction becomes impermeable ($\phi_1 \to 0$), porosity cannot move into an impermeable region but must accumulate at the boundary until the amplitude of the wave $\to \infty$ or the matrix disaggregates. For all numerically resolvable values of ϕ_1, the excess upstream melt flux is always accommodated in a series of non-zero-wavelength porosity waves; therefore, the wavetrain grows in length with time. If the phase velocity of the leading wave is slower than the growth rate of the wavetrain, then each new wave forms further and further back relative to the matrix. This 'back-propagation' can be seen clearly in figure 3 for $\phi_1 = 0.2$. Each of the solitary waves actually moves forward; however, it is information about variations in melt flux that moves backwards. Back-propagation of information is a ubiquitous feature of this solution for problems with $\phi_1 \lesssim 0.5$ but is most noticeable for small ϕ_1. For $\phi_1 \gtrsim 0.5$, the well-developed waves move forward faster than the wavetrain grows. For $\phi_1 = 0.8$, the region near the original shock front ($z \sim 60$–120) eventually approaches a steady state with $\phi = 1$. The back-propagation appears to be robust and may have significant implications for the long-term behaviour of flow in deformable porous media. Inspection of figure 3 shows that if the wavetrain continues to grow indefinitely, then the region near the initial obstruction ($z \gtrsim 50$) will never go to steady state. More generally, information about obstructions in the flow at boundaries can propagate into the interior with unknown results.

3.2. *Fidelity of solution and simple physics of dispersion*

The general behaviour of this solution appears to be a growing, dispersive train of porosity waves that behave locally as solitary waves. It is important, however, to

---

† It should be noted that the phase velocity (4) depends only on A and the minimum porosity ϕ_1. Inspection of figure 3 shows that, except for the leading wave, the minimum porosity immediately preceding each wave can be significantly greater than ϕ_1. This limited interaction between waves is typical of the solitary waves (Scott & Stevenson 1984; Barcilon & Richter 1986).
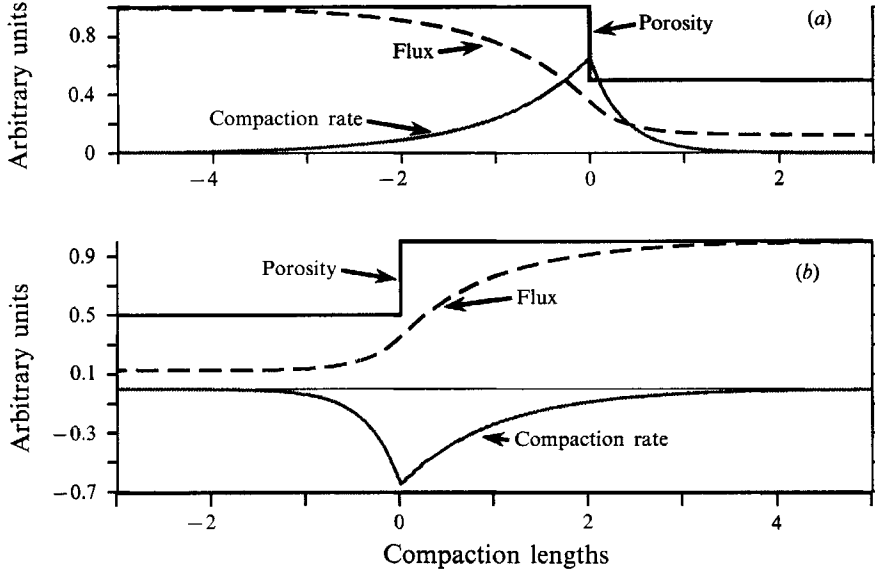
M. Spiegelman

FIGURE 6. (a) Initial compaction rate and separation flux for a decreasing step in porosity showing how viscous resistance distributes the compaction rate (pressure) into two decaying exponentials away from the discontinuity. Because $\mathscr{C} = \partial\phi/\partial t > 0$ in regions where $\partial\phi/\partial z = 0$, viscous resistance causes the porosity to grow both forwards and backwards of the initial shock. (b) When the step is reversed so that the flux increases in the direction of flow, viscous stresses cause the porosity to decrease and form a minimum.

demonstrate that these results are accurate and consistent with the form of the governing equations. Numerically, these results are robust. Changing the grid size, time step, n and even the numerical scheme does not alter the rank ordering, dispersion and back-propagation of solitary waves. The leading porosity waves have already been shown to behave as solitary waves and these codes can accurately reproduce the analytic solitary wave solutions to within 0.2% in amplitude and velocity (see Appendix A). Figure 5(b) shows that in amplitude and phase velocity, the results of the different runs are completely distinct and that even numerical errors of the order of a few percent within a given run will not change the overall relationship between runs.

It is also possible to show that some of the features of these solutions, such as the lack of permanent form, the formation of porosity extrema, and rank ordering are consistent with the form of the governing equations and boundary conditions. Following the analysis of Barcilon & Richter (1986) for one-dimensional solitary waves with $n = 3$ and $\phi_0 \ll 1$, Appendix B shows that no solutions of permanent form and constant phase velocity exist which satisfy the boundary conditions

$$\left.\begin{aligned}
\phi(\infty) &= \phi_1, & \phi(-\infty) &= 1, \\
\mathscr{C}(\infty) &= 0, & \mathscr{C}(-\infty) &= 0, \\
\mathscr{C}_z(\infty) &= 0, & \mathscr{C}_z(-\infty) &= 0,
\end{aligned}\right\} \tag{5}$$

if $\phi(\infty) \neq \phi(-\infty)$ (i.e. solitary waves are the only waveform of permanent shape and constant speed where the compaction rate $\mathscr{C}$ vanishes at $\pm\infty$).

To show that the elliptic compaction term produces porosity extrema and causes information to propagate away from the shock, consider the initial compaction rate field for a step in porosity. Figure 6(a) shows a step decrease in porosity where

$\phi = 1$ for $z < 0$ and $\phi = \phi_1$ for $z > 0$. Given this initial condition, neglecting melting and assuming $\phi_0 \ll 1$, the one-dimensional compaction rate equation (Part 1, equation (42)) at $t = 0$ becomes

$$-\partial^2 \mathscr{C}/\partial z^2 + \mathscr{C} = 0, \quad z < 0,$$
$$-\delta_1^2 \partial^2 \mathscr{C}/\partial z^2 + \mathscr{C} = 0, \quad z > 0, \tag{6}$$

where $\delta_1 = \phi_1^{n/2}$ is the compaction length in the region $z > 0$. Using the boundary conditions that the compaction rate vanishes at $\pm\infty$, together with the matching condition that $\mathscr{C}$ (and the melt flux) is continuous at $z = 0$, and the global mass conservation constraint that

$$\int_{-\infty}^{\infty} \mathscr{C}\,\mathrm{d}z = \int_{-\infty}^{\infty} -\frac{\partial}{\partial z}\phi(v - V)\,\mathrm{d}z = (1 - \phi_1^n) \tag{7}$$

equations (6) have solutions

$$\mathscr{C}(z, 0) = \begin{cases} \mathscr{C}_{\max}\,\mathrm{e}^z, & z < 0 \\ \mathscr{C}_{\max}\,\mathrm{e}^{-z/\delta_1}, & z > 0 \end{cases} \tag{8}$$

where
$$\mathscr{C}_{\max} = (1 - \phi_1^n)/(1 + \delta_1).$$

Figure 6(a) shows profiles of ϕ, $\mathscr{C}$, and the separation flux $q = k_\phi(\mathscr{C}_z - 1)$ for $n = 3$, $\phi_1 = 0.5$. While the porosity is discontinuous, the flux varies smoothly. Moreover, the compaction rate is finite and is distributed in two decaying exponentials both upstream and downstream of the shock. In these simple problems, $\mathscr{C} = \partial\phi/\partial t$; therefore, the initial evolution of this step will be for porosity to grow locally around the shock. The larger the jump in flux, the greater the maximum growth rate, $\mathscr{C}_{\max}$, and the more that this growth occurs behind the shock front. As $\phi_1 \to 0$, the growth rate at the shock approaches a maximum, all of the growth occurs upstream of the shock, and the waveform cannot propagate into the impermeable region. These results should be compared to the zero-compaction-length approximation where both the porosity and the flux are discontinuous, and the compaction rate is simply a travelling Dirac delta function $\mathscr{C} = (1 - \phi_1^n)\delta(z - c_s t)$. Moreover, in the zero-compaction-length approximation, shocks can propagate even into impermeable regions. This analysis shows that viscous stresses distribute the effects of rapid flux changes away from the shock, can produce local maxima, and provide a physical mechanism for both forward and backward propagation of porosity variations.

The preceding argument shows that the pressure gradients due to viscous volume changes of the matrix causes a porosity maximum to develop around a step decrease in porosity. The key to forming dispersive wavetrains, however, is the ability for local porosity minima to form directly behind the flux maximum. If we reverse the direction of the porosity jump and let $z \to -z$ (figure 6b), then the same analysis used to derive (8) shows that an initial step increase in porosity will lead to a local minimum as the rapid increase in flux drains melt from the low-porosity region upstream. While this analysis is too simple to show that a dispersive wavetrain of solitary waves is the preferred solution for this initial condition, it suggests that the elliptic term produces an oscillating porosity profile by alternately obstructing and draining regions of variable flux. This suggestion is supported by close examination of figure 2. It should also be noted that without melting or matrix shear, the only waveform that propagates without growing is one where the melt flux increases linearly with porosity ($\mathscr{C} \propto \partial\phi/\partial z$). Appendix B shows that this property is an alternative definition for the solitary waves.

Finally, the apparent rank ordering of the wavetrains is consistent with the weak constraint provided by (7) that the integral of the compaction rate must be constant and positive for the boundary conditions of this problem. Thus, if $\mathscr{C}$ oscillates about zero (figure 3), the compaction rate in expanding regions must be somewhat larger than in compacting regions. A series of well-separated solitary waves have $\int \mathscr{C} \sim 0$ because $\mathscr{C}$ is antisymmetric in a solitary wave (indeed $\mathscr{C} = -c\phi_z$). The integral of the compaction rate also vanishes for the periodic wavetrains of Olson & Christensen (1986).

3.3. *A simple physical argument for* $A(\phi_1)$

The preceding arguments support the observation that viscous resistance of the matrix to volume changes causes larger obstructions to produce larger slower-moving solitary waves. This analysis, however, is not sufficient to predict the amplitude of the solitary waves that eventually develop. Ideally, a method analogous to the inverse scattering transform for solitons would be of great use for calculating the evolution of arbitrary initial conditions. These solitary waves, however, are not solitons and it is not clear that such a method exists. This section presents a simple physical argument based on conservation of mass that reproduces much of the trends of figures 4(a) and 5(b) surprisingly well.

This argument is similar to that used to calculate the speed of the shock in the zero-compaction-length approximation. Now, it might be expected that the leading wave would simply grow to the solitary wave that moves at the phase velocity of the shock. If this were the case, then (4) and the shock speed for $n = 3$ give

$$A_s(\phi_1) = (1 + \phi_1)/2\phi_1, \quad c_s(\phi_1) = 1 + \phi_1 + \phi_1^2. \tag{9}$$

This relationship is shown as the dashed curve in figures 4(a) and 5(b). While it is a reasonable approximation for the maximum amplitude and phase velocity for small shocks ($\phi_1 > 0.5$), this argument overestimates the amplitude and phase velocity for $\phi_1 < 0.5$ beyond any possible numerical error. It is interesting to note that the calculations that display back-propagation have maximum phase velocities $c_{max} < c_s$ (although this may be coincidental).

While the wavetrain does not move at the speed of the shock, it does appear to move with the mass of the shock. To show this, we extend the standard argument used to calculate the shock speed. Figure 7 summarizes the basic argument. Consider a perfect step-function shock at $z = 0$, $t = 0$. At time Δt, the characteristic solution actually predicts a breaking porosity wave (figure 7a) which is physically unrealistic as the porosity cannot be triply valued. The position of the shock front at time Δt is calculated in the standard way (Whitham 1974), by conserving mass and determining the position of the step function that contains the same volume of porosity as does the breaking wave (figure 7b). The excess porosity in the breaking wave at $t = \Delta t$ is

$$V_b = (1 - \phi_1^n)\Delta t \tag{10}$$

while the excess volume of a step function travelling at constant phase velocity c_s is

$$V_s = (1 - \phi_1)c_s\Delta t. \tag{11}$$

Setting the volumes equal yields the shock speed $c_s = (1 - \phi_1^n)/(1 - \phi_1)$.

While a step function is a poor approximation to the porosity profile when viscous resistance is significant, this argument can be extended to find the amplitude of the solitary wave that contains the same excess volume as the breaking wave (figure 7c). The only uncertainty in this argument arises from the fact that the excess volume of the breaking wave depends on the time of formation Δt. Examination of figure 7(c),
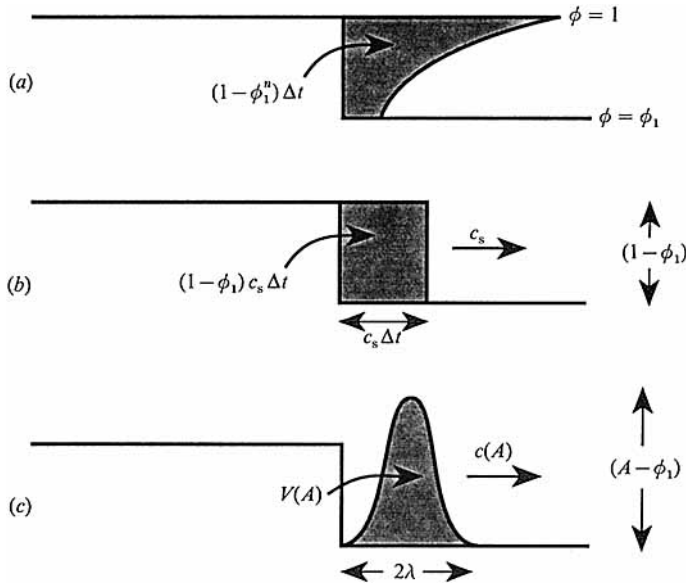
FIGURE 7. Schematic illustration of a simple physical argument to estimate the amplitude of solitary waves as a function of the amplitude of the predicted shock. All arguments assume an initial step function ($\phi_{max} = 1$, $\phi_{min} = \phi_1$) at $t = 0$. (*a*) Characteristic 'breaking wave' solution. At $t = \Delta t$ the excess porosity in the breaking wave is $l_b = (1 - \phi_1^u)\Delta t$. This solution is unrealistic as porosity cannot be multiply valued. (*b*) Shock solution: the excess porosity V_b is accommodated in a step-function shock that travels at the constant phase velocity $c_s = (1 - \phi_1^u)/(1 - \phi_1)$. (*c*) Scaling argument: solitary wave solution. Excess porosity is accommodated in a solitary wave of amplitude A. The characteristic time for forming the solitary wave is approximately $\Delta t = 2\lambda(A)/c(A)$.

however, suggests that a reasonable estimate for Δt is the time it takes a fully formed wave to move its full wavelength. That is $\Delta t \approx 2\lambda/c$, where λ is an estimate of the half-wavelength of the solitary wave. Appendix B provides a reasonable definition of λ. As the volume, wavelength, and speed of a solitary wave all depend on the amplitude A, ϕ_1, and n, setting the volume of the solitary wave equal to V_b and fixing n yields the implicit relationship between A and ϕ_1:

$$1 - \phi_1^n = V(A, \phi_1, n) \, c(A, \phi_1, n)/[2\lambda(A, \phi_1, n)]. \tag{12}$$

V, c and λ have analytic expressions if $n = 3$ (Appendix B) and the relation $A(\phi_1)$ is readily found. This relationship is plotted in figures 4(*a*) and 5(*b*). Comparing it to the range of amplitudes produced at $t = 80$ shows that this argument provides a good estimate for the mean amplitude of the wave train. This argument is consistent with the basic behaviour of these solutions and conservation of mass. Until more sophisticated techniques are developed, this method forms a simple parameterization of the numerical results.

4. Effects of melting

The previous examples demonstrate how viscous stresses in the matrix cause a simple step shock to disperse into solitary waves when there are no melting source terms. These problems also show a simple physical correspondence between the prediction of shocks and the production of solitary waves for a step shock of

permanent form and constant speed. By including the effects of melting (and freezing) we can show that this relation is applicable even when the predicted shock has a time-dependent amplitude. While the solitary waves are no longer of permanent form, the following example suggests that they simply adjust to local variations in melt flux.

Section 4.5 of Part 1 describes how melting modifies the behaviour of step-function shocks. The geometry of the model problem we consider here follows that of figure 7 of Part 1, where an initial porosity step propagates into a nearly constant melting rate zone given by

$$\Gamma(z) = \Gamma_0 \begin{cases} \text{sech}^2\left((z-z_0)/\lambda\right), & z < z_0, \\ 1, & z_0 < z < z_{\mathrm{m}}, \\ \text{sech}^2\left((z-z_{\mathrm{m}})/\lambda\right), & z_{\mathrm{m}} < z. \end{cases} \tag{13}$$

Again, the discontinuous melting rate field has been smoothed slightly ($\lambda = 1$) to avoid numerical artifacts. Given Γ_0 and setting $W_0 = 0$, the porosity trajectories predicted by the zero-compaction-length approximation are

$$\begin{aligned} \phi_{\max}(z) &= \left[1 + \frac{\rho_{\mathrm{s}}}{\rho_{\mathrm{f}}}\int \Gamma \, \mathrm{d}z\right]^{1/n}, \\ \phi_{\min}(z) &= \left[\phi_1^n + \frac{\rho_{\mathrm{s}}}{\rho_{\mathrm{f}}}\int \Gamma \, \mathrm{d}z\right]^{1/n} \end{aligned} \right\} \tag{14}$$

(see figure 7 of Part 1). For this problem we fix $(z_{\mathrm{m}} - z_0) = 50$, $n = 3$, $\phi_1 = 0.2$ and choose Γ_0 such that the shock would enter the melting zone with a minimum porosity ϕ_1 and exit as a smaller-amplitude shock with a normalized minimum porosity, ϕ_1. By choosing ϕ_1' such that

$$\phi_1' = \lim_{z \to \infty} \frac{\phi_{\min}(z)}{\phi_{\max}(z)} = 0.2, 0.3, \ldots, 0.8 \tag{15}$$

the results of this problem can be compared directly to those of §3 where there was no melting. Using (13) and (15), Γ_0 is given by

$$\Gamma_0 = \frac{\rho_{\mathrm{f}}}{\rho_{\mathrm{s}}(1 + 2\lambda/z_{\mathrm{m}})}\left[\frac{\phi_1'^n - \phi_1^n}{1 - \phi_1'^n}\right]. \tag{16}$$

The initial conditions for the porosity in figure 8 are simply a superposition of the smoothed step given by (2), and $\phi_{\min}(z)$. In the zero-δ approximation, $\phi_{\min}(z)$ is a stable steady-state profile. Therefore, the melting zone and the region above should be initially in steady state. In this model problem, the wavetrain will develop as before for 25 compaction lengths and then enter the melting zone. Boundary conditions are free flux on both boundaries, which are placed far from regions of varying flux.

4.1. *Results*

Figure 8 shows the evolution of this initial condition for a small melting rate ($\phi_1' = 0.4$) and a larger melting rate ($\phi_1' = 0.7$). In both cases, as each porosity wave moves through the melting region, its amplitude decreases while the wavelength and phase velocity increase. These effects are more pronounced for large melting rates. This behaviour is consistent with the effects of melting on shocks in the zero-compaction-length approximation. Figure 7 of Part 1 shows that, for this initial condition, melting decreases the amplitude of the shock, increases the minimum porosity (and
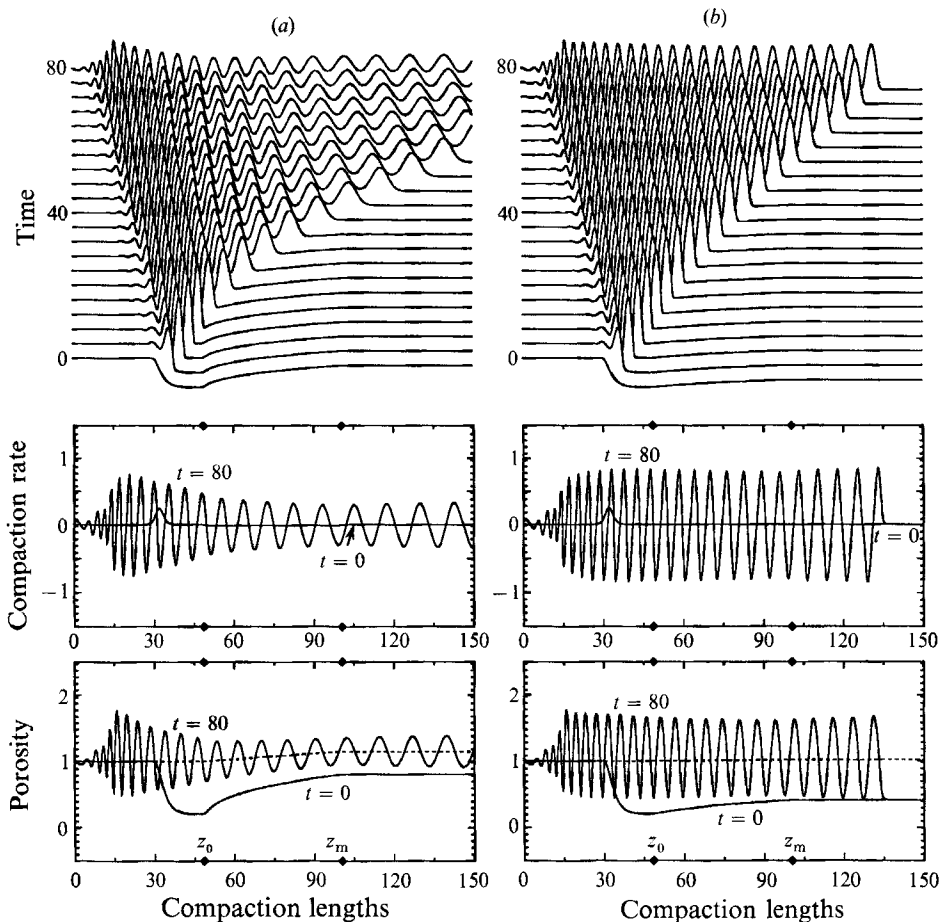
FIGURE 8. The effect of melting on the porosity waves. These plots show porosity profiles *vs.* time, as well as initial and final porosity and compaction rate profiles. (*a*) Porosity and compaction rate for a rapid melting rate ($\Gamma_0 = 4.16 \times 10^{-1}$, $\phi'_1 = 0.7$). Melting occurs in a region 50 compaction lengths long between z_0 and z_m. There is no melting outside this region. There are free-flux boundary conditions at $z = 0$ and 220. The figure is plotted to $z = 150$, however, for comparison to the slow melting solution. (*b*) Porosity and compaction rate profiles for a slower melting rate ($\Gamma_0 = 4.88 \times 10^{-2}$, $\phi'_1 = 0.4$). In both calculations, the initial condition for $z < z_0$ is the same as in figure 3(*a*). Increasing the melting rate causes waves to broaden, accelerate, and decrease in amplitude as they pass through the melting zone. The dashed curve is the steady-state solution for ϕ_{max} calculated from the zero-δ approximation.

therefore the minimum compaction length) and increases the speed of the shock. Scott & Stevenson (1986) also note that melting causes solitary waves to decrease in amplitude. However, more careful analysis shows that the waves simply evolve to the waves that accommodate the local differences in fluid flux.

Figure 9(*a*) shows the amplitude of the leading wave with time for various degrees of melting. While melting decreases the absolute amplitude of the porosity wave (as well as the rescaled amplitude $A' = A(z,t)/\phi_{max}(z)$), the leading wave still behaves locally as a solitary wave. The theoretical phase velocity of a solitary wave of amplitude $A(t)$ and minimum porosity $\phi_{min}(z_p)$ is

$$c'(A, \phi_{min}) = \phi_{min}(z_p)\,(2A + \phi_{min}(z_p)), \tag{17}$$
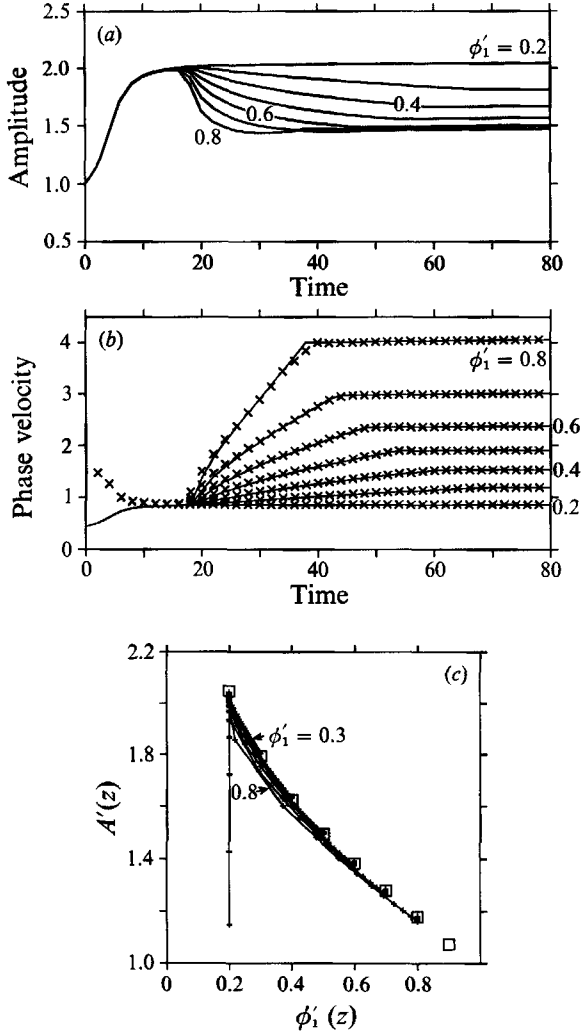
FIGURE 9. The effect of melting on the leading porosity wave. (*a*) Absolute amplitude of the leading wave as a function of time. Up to $t \sim 16$, all runs produce similar amplitudes. The overall decrease in amplitude is caused primarily by the decreasing difference in melt flux between ϕ_{max} and ϕ_{min}. The small increase in amplitude for $\phi'_1 = 0.8$ is due to ϕ_{min} increasing faster than the step amplitude decreases. (*b*) Phase velocity of the leading wave as a function of time: $\times$, the measured velocities of the leading porosity maximum (see figure 5*a*); the solid curve is the theoretical phase velocity of the solitary wave with amplitude $A(t)$ and minimum porosity $\phi_{min}(z_p(t))$. (*c*) Renormalized amplitude of the leading wave, $A'(z) = A_{max}(z)/\phi_{max}(z)$, as a function of the renormalized minimum porosity, $\phi'_1(z) = \phi_{min}(z)/\phi_{max}(z)$. $\phi'_1 = 0.2, ..., 0.8$. $\square$, The amplitudes of the leading waves, $A_{max}(\phi_1)$, at $t = 80$ from the previous calculations where there was no melting. $A'(\phi'_1)$ is similar to $A(\phi_1)$, for all melting rates. This result shows that porosity waves adjust to the local shock amplitude. The largest discrepancy occurs at large melting rates ($\phi'_1 = 0.8$) when the leading wave just enters the melting region. In this region ϕ'_1 changes rapidly and is underestimated.

where z_p is the position of the leading wave crest at time t. Figure 9(*b*) compares the theoretical velocity with the measured phase velocity of the leading wave. Once the leading wave is well formed, the fit is quite good. Moreover, the leading wave appears to adjust to the solitary wave that corresponds to the local shock amplitude. In the
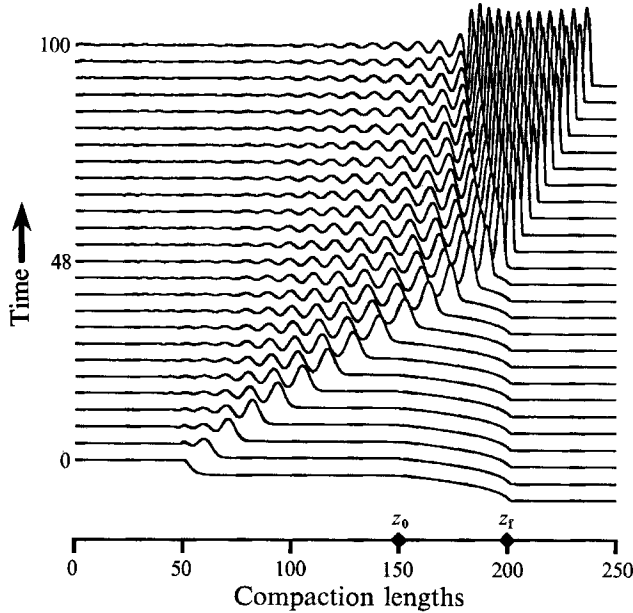
FIGURE 10. The effect of freezing on porosity waves. This geometry is similar to that of figure 8 but is reversed so that a small shock with $\phi_1' = 0.7$ enters a constant-freezing-rate zone that extends from $z_0 - z_f$, ($\Gamma_0 = -4.16 \times 10^{-1}$, $z_f - z_0 = 50$) and exists as a shock with $\phi_1 = 0.2$. This plot shows porosity profiles *vs.* time. As the porosity trajectories decrease and diverge, the amplitude of the solitary waves increases while their wavelength and velocity decrease. Note the back-propagation of large-amplitude solitary waves near the top of the freezing zone.

previous solution, where there was no melting, the amplitude of the leading wave depended only on the minimum porosity ϕ_1. If this relationship applies when the predicted shock amplitude is time dependent, it is expected that $A'_{max}(\phi_1') \approx A_{max}(\phi_1)$ where

$$ A'_{max} = \frac{A_{max}(z_p)}{\phi_{max}(z_p)}, \quad \phi_1' = \frac{\phi_{min}(z_p)}{\phi_{max}(z_p)}. \tag{18} $$

This relationship is shown in figure $9(c)$ for the leading wave. In nearly all the calculations, $A'(\phi_1')$ is within a few percent of $A_{max}(\phi_1)$. The largest discrepancies occur at higher melting rates near the base of the melting zone where ϕ_{min} increases rapidly over a few compaction lengths. However, as long as melting causes the flux to change over a lengthscale larger than the wavelength of the solitary waves, then the waves appear to behave 'adiabatically'.

4.2. *Effects of freezing*

In the zero-compaction-length approximation, the porosity trajectories $\phi(z, q_m)$ for melting and freezing are identical under the transformation $\Gamma \to -\Gamma$ and $z \to -z$. Thus, for many problems, the effects of freezing should simply be the reverse of those caused by melting. Figure 7 of Part 1 shows the behaviour of a shock with minimum porosity ϕ_1 passing through a melting zone. By simply reversing the direction of motion, this figure would just as easily demonstrate a shock of minimum porosity ϕ_1' moving into a freezing zone. Figure 10 shows this initial condition for $\phi_1' = 0.7$, $\phi_1 = 0.2$. As expected, the amplitude of the porosity waves increases and their speed decreases as the porosity trajectories diverge. This example indicates that while

melting decreases the amplitude of solitary waves, the process may be reversible and freezing can actually amplify small perturbations in the flux. If freezing continues to the point where the matrix becomes impermeable ($\phi_1 \to 0$, $k_\phi \propto \phi$), then the waves will grow until the matrix disaggregates or other forms of transport, such as crack formation, become important. This example demonstrates the effects of freezing when it occurs over many compaction lengths. When freezing occurs on a lengthscale comparable to the compaction length, it can also cause high-porosity channels to form (Sparks & Parmentier 1991; Spiegelman 1990, 1991). These channels arise from the obstruction in flux caused by the frozen impermeable boundary. The channels are similar to the solitary waves in cross-section and develop into a rank-order set of channels that spread out from the freezing boundary. The only significant difference between these channels and the wavetrains shown here is that the channels do not propagate into the freezing region.

5. Discussion

The purpose of these model problems is to demonstrate and quantify how viscous resistance of the matrix to volume changes modifies the simple shock solutions predicted using the zero-compaction-length approximation. The initial response of the elliptic term is to cause fluid to accumulate in local porosity maxima near obstructions in the flux. These porosity maxima, however, appear to drain fluid from the region surrounding them, producing new obstructions that excite the formation of additional porosity waves. Thus, while viscous resistance is initially significant only in narrow boundary layers, the growth of the solitary waves allows information to propagate many compaction lengths away from the original obstruction. For some initial conditions, it was shown that information can propagate backwards relative to the matrix even though both the fluid and porosity propagate forwards. The equations governing volume changes of the matrix are extremely time dependent and any perturbation to steady-state solutions is likely to shed solitary waves. For the problems shown here, there is a clear correspondence between the magnitude of the obstruction in the flux and the amplitude of the solitary waves that are produced. Large obstructions produce large-amplitude slow-moving wavetrains while smaller obstructions produce small-amplitude wavetrains. When mass transfer between solid and liquid is included, the solitary waves are no longer of permanent form; however, melting and freezing do not change the quantitative relationship between the amplitude of the predicted shock and the amplitude of the solitary waves that are produced. The general conclusion of this work is that viscous resistance to volume changes must be included for an accurate description of flow in viscously deformable porous media. As with many elliptic equations, a small compaction length does not imply a negligible compaction term.

For clarity, accuracy and ease of analysis, this paper has considered only one-dimensional problems in the limit of small porosity where the permeability exponent is $n = 3$. While relaxing these conditions will change the quantitative results and allow for new processes such as matrix convection, the results presented here and in Part 1 suggest that the general correspondence between the prediction of shocks and the production of solitary waves should carry through to more complicated problems. Spiegelman (1989) considers the evolution of porosity steps when the permeability exponent is $n = 2$, and produces results that are qualitatively identical to the problem with $n = 3$. The porosity waves, however, travel at the speed of the $n = 2$ solitary waves. Preliminary results using a permeability exponent of $n = 1$ also
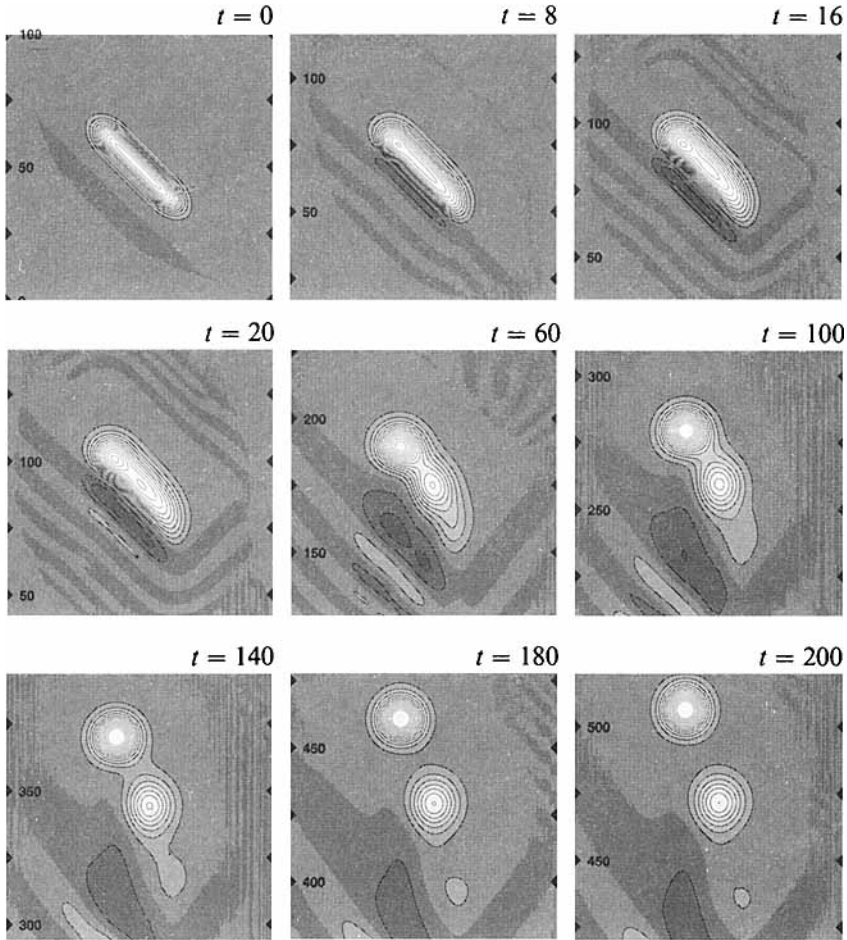
FIGURE 11. Evolution of a two-dimensional region of excess porosity that is inclined at 45°. This initial condition disperses into approximately three rank-ordered two-dimensional solitary waves and a small-amplitude dispersive background. Unlike the one-dimensional problems, here the permeability exponent $n = 2$. Initial amplitude $A = 1.5$ times the background porosity (dimensionless $\phi = 1$). Contour interval for porosity is 0.04. Lighter grey shades indicate excess porosity ($\phi > 1$). $\phi < 1$ in darker regions. The box size is 100×100 compaction lengths (200×200 grid) but the compaction length is scaled to the minimum background porosity. Figures are shown in a moving frame ($V_0 = 2.1k$).

break up into porosity extrema; however, the waves are no longer of permanent form as there is no nonlinear steepening term to balance the viscous dispersion. Figure 11 shows the evolution of a local two-dimensional region of excess porosity for a problem with permeability $k_\phi \propto \phi^2$. This initial condition disperses into three cylindrically symmetric two-dimensional solitary waves and a dispersive tail. Solitary wave solutions have been shown to exist in all dimensions (Scott & Stevenson 1986; Barcilon & Lovera 1989) and the viscous resistance term must be responsible for the permanent form of the solitary waves. Otherwise, the waves would continue to steepen into shocks. As the zero-compaction-length approximation allows for shock solutions in all dimensions, it is tempting to speculate that, in general, any initial condition that predicts shocks in the zero-compaction-length approximation will produce solitary waves in the full equations.

If the relationship between shocks and solitary waves holds for more complicated problems then the zero-compaction-length approximation becomes a straightforward test for determining if, when and where solitary waves should form. By extending the parameterization between the amplitudes of shocks and solitary waves, it may also be possible to estimate which waves will be produced. Accurate numerical resolution of the waves, however, requires that the smallest compaction length in the obstruction is adequately resolved. This resolution requirement places strong limits on the problems that are presently numerically feasible (as an example, figure 3 a ($\phi_1 = 0.2$) requires 6000 grid points in one dimension). In addition, some care must be taken in the choice of initial and boundary conditions. Because of the strong time dependence of these equations and the potential for some solutions to have no steady solution, the choice of initial condition is critical. Nevertheless the zero-compaction-length approximation provides a framework for predicting and interpreting time-dependent problems. This approximation has already proved useful for gaining insight into the possible processes occurring in natural viscous two-phase systems and suggests that processes such as magma migration should be inherently episodic in space and time.

Appendix A. Numerical methods: accuracy and resolution criteria

Proper resolution of the solitary waves requires that the compaction rate is well resolved in the region of small porosity preceding the wave. Quantitatively, this means using a grid spacing fine enough to resolve the compaction length of the smallest porosity. This is justified by the analysis of §3.2 that shows that in the region of nearly uniform porosity ϕ_1 preceding the wave, the compaction rate decays exponentially into the constant-porosity region with a lengthscale of δ_1, the compaction length for $\phi = \phi_1$. In practice it was found that 5 grid points per smallest compaction length ($\Delta z = \frac{1}{4}\delta_1$) gave accurate solutions with a minimum of round-off error (see below). For stability and accuracy, the time step must satisfy the Courant condition

$$\Delta t/\Delta z \leqslant 1/c_{\max},$$

where $c_{\max}$ is the phase speed of the fastest solitary wave. In practice, $\Delta t/\Delta z = 1/(2c_{\max})$ was found to be adequate.

The numerical schemes have been tested against the analytic solitary wave solution for $n = 3$, $W_0 = 0$, $\Gamma = 0$ in the small-ϕ_0 approximation. Properties of these waves are given in Appendix B. For the code to be accurate, the solitary waves should travel without change of shape at a constant phase velocity. The code was tested for waves of amplitude 2, 5 and 10 times the homogeneous small background porosity. Each run was conducted for times sufficient for the wave to travel at least ten full wavelengths.

Results of these tests are shown in figure 12. This figure shows the effects of changing the time step and grid spacing on waves of different amplitudes. These plots show the normalized error in amplitude and phase velocity with time. In general, this
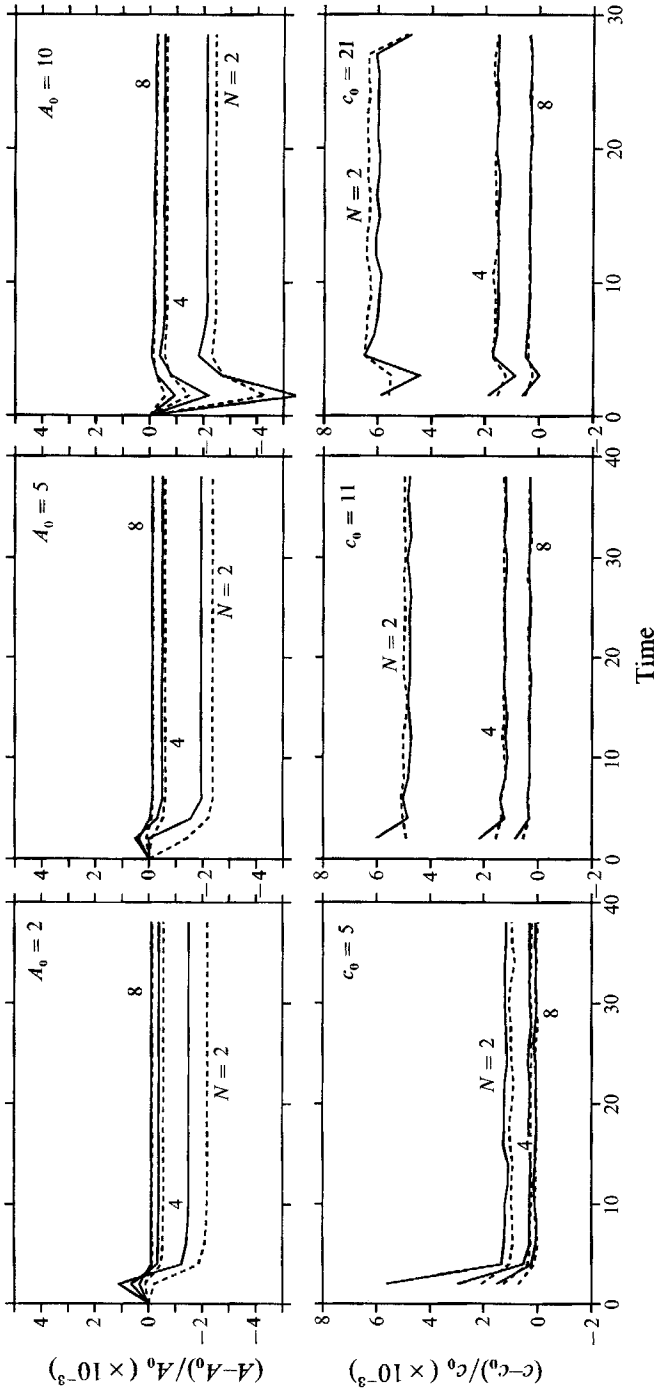
FIGURE 12. Results of accuracy tests of the numerical method for the evolution of analytic solutions for solitary waves ($n = 3$, $\phi_0 \ll 1$, Appendix B). A_0 is the theoretical amplitude of the solitary wave that travels over a uniform background porosity, $\phi = 1$. For $n = 3$, $c_0 = 2A_0 + 1$. The plots show the differential error in amplitude $(A(t) - A_0)/A_0$, and phase velocity $(c(t) - c_0)/c_0$ as a function of time for solitary waves with $A_0 = 2, 5, 10$. For each wave, runs were conducted with grid step, $\Delta z = 1/N$, $N = 2, 4, 8$ (i.e. 0.5–0.125 times the smallest compaction length). Time steps are $c_0 \Delta t / \Delta z = 0.5$ (solid) and 0.25 (dashed). The plots show that the accuracy is insensitive to the time step and improves rapidly for increasing spatial resolution. The plots also show the effects of wave amplitude on the accuracy of the scheme. For moderate-amplitude waves, $N = 4$ maintains amplitude to $\sim 0.1\%$, phase velocity to $\sim 0.2\%$.

scheme is sufficiently accurate to resolve the first-order variations in amplitude and phase velocity demonstrated by the dispersive shock problem (§3). These schemes are not sensitive to the choice of time step and show a second-order improvement in accuracy with decreasing grid spacing as might be expected from centred differencing. Errors for poorly resolved waves ($N = 2$) increase rapidly as the amplitude of the wave increases; however, solutions with finer meshes are hardly affected. All model problems in this paper use 5 grid points per smallest compaction length ($N = \delta_1/\Delta z = 4$) and $\Delta t/(c_0 \Delta z) = 0.5$ (solid curves). Neglecting the initial discretization error, this choice of numerical parameters produce errors in amplitude that are less than 0.1 % and errors in phase velocity that are less than 0.2 %. This result should be compared to variations in amplitude of 10–40 % between individual waves produced in any given run of §3.

Appendix B. Properties of solitary waves: small-ϕ_0 approximation

The general derivation for solitary waves of permanent form and constant phase velocity in the small-ϕ_0 approximation is given in Scott & Stevenson (1986) and Barcilon & Richter (1986). This appendix presents some additional properties of these waves.

Using the notation of Barcilon & Richter, f is the dimensionless porosity scaled to the value of the background porosity (i.e. $f = 1$ is $\phi = \phi_1$ in the shock experiments) and $\zeta = z - ct$ is the distance coordinate in a frame moving at constant speed c. In this frame the compaction rate satisfies $\mathscr{C} = -cf'$ (primes denote differentiation with respect to ζ) and can be written as a function of porosity as

$$\mathscr{C}^2 = \frac{-2c}{f^{n-1}}\left[f^n - \frac{(n^2 - 2n + c)}{(n-1)(n-2)}f^{n-1} + \frac{c}{n-2}f - \frac{c-1}{n-1}\right] \quad \text{(B 1)}$$

for $n > 2$, and $\quad \mathscr{C}^2 = (-2c/f)[f^2 + (c-2) - cf\ln f - (c-1)] \quad$ (B 2)

for $n = 2$. For $n = 3$, $(f-1)^2$ can be factored out to yield

$$\mathscr{C}^2 = \frac{-2c(f-1)^2}{f^2}[f - \tfrac{1}{2}(c-1)]. \quad \text{(B 3)}$$

The dispersion relation, $c(A)$, is found by requiring $\mathscr{C}(A) = 0$, where A is the maximum porosity of the solitary wave. For $n = 2$

$$c(A) = (A-1)^2/[A \ln A - (A-1)]. \quad \text{(B 4)}$$

For $n = 3$ $\qquad\qquad\qquad\qquad c(A) = 2A + 1, \qquad\qquad\qquad\qquad$ (B 5)

and for general integer $n \geqslant 3$

$$c(A) = (n-2)P_{n-2}(A)/P_{n-3}(A) \quad \text{(B 6)}$$

where $\qquad\qquad P_{n-2}(f) = \sum_{j=0}^{n-2}(j+1)f^j, \quad P_{n-3}(f) = \sum_{j=0}^{n-3}(n-2-j)f^j.$

Note for all $n \geqslant 2$, $c(1;n) = n$ and therefore all waves travel at least n-times faster than the background flux in the pores.

The waveform $f(\zeta; A, n)$ of a solitary wave is given implicitly by

$$\zeta(f;n) = -c\int_A^f \frac{\mathrm{d}f}{\mathscr{C}(f;n)}. \quad \text{(B 7)}$$
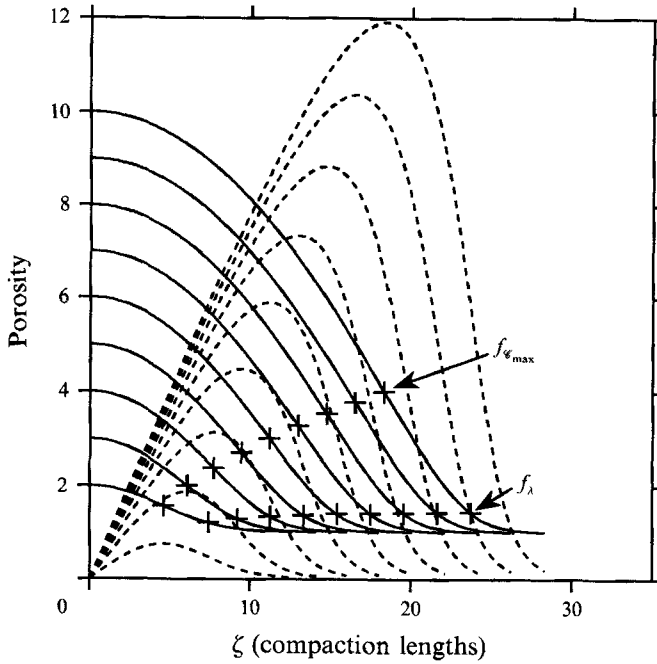
FIGURE 13. Porosity (solid) and compaction rate (dashed) profiles for $n = 3$, $A = 2$–10. Critical points are shown by $+$. $f_{\mathscr{C}_{max}}$ is the porosity where $\mathscr{C}$ has a maximum. f_λ is the porosity where $\mathscr{C}'' = 0$ ($f''' = 0$). The porosity is symmetric about $\zeta = 0$. The compaction rate is antisymmetric $\mathscr{C} = -cf'$.

For $n = 3$ this integral is analytic and yields upon integration

$$\zeta = (A + \tfrac{1}{2})^{\frac{1}{2}} \left[-2(A-f)^{\frac{1}{2}} + \frac{1}{(A-1)^{\frac{1}{2}}} \ln\left(\frac{(A-1)^{\frac{1}{2}} - (A-f)^{\frac{1}{2}}}{(A-1)^{\frac{1}{2}} + (A-f)^{\frac{1}{2}}} \right) \right]. \tag{B 8}$$

This solution is given by Barcilon & Richter (1986) and Richter & McKenzie (1984) and is plotted in figure 13 together with the compaction rate for $n = 3$

$$\mathscr{C}(f) = (2c)^{\frac{1}{2}} \frac{(f-1)}{f} (A-f)^{\frac{1}{2}}. \tag{B 9}$$

Examination of figure 13 shows that there are several useful critical points for the solitary waves. Besides the obvious, $f = A$, $\mathscr{C} = 0$, there are the extrema of the compaction rate $\mathscr{C}_{max}$ where $\mathscr{C}' = 0$. Using $\mathscr{C} = -cf'$ gives

$$\mathscr{C}' = -(1/f^n)[f^n - cf + c - 1]$$

$$= -\frac{(f-1)}{f^n} \left[\sum_{m=0}^{n-1} f^m - c \right] \tag{B 10}$$

which has zeros at $f = 1$ and the single real root of the polynomial in brackets. For $n = 2$

$$f_{\mathscr{C}_{max}}(A) = c(A) - 1, \tag{B 11}$$

and for $n = 3$ $\qquad f_{\mathscr{C}_{max}}(A) = \tfrac{1}{2}[(1 + 8A)^{\frac{1}{2}} - 1]. \tag{B 12}$

A useful measure of the wavelength of a solitary wave is the porosity for which $\mathscr{C}''$ vanishes. For general n this value is

$$f_\lambda(A ; n) = n(c-1)/c(n-1). \tag{B 13}$$

A	1	2	5	10	20	30
$V(f_{\mathscr{C}_{\max}},A)/V(1,A)$	0.8165	0.7365	0.8753	0.9331	0.9651	0.9764
$V(f_\lambda,A)/V(1,A)$	0.8165	0.9302	0.9850	0.9958	0.9989	0.9995

TABLE 1. Ratio of excess volume at $f = f_{\mathscr{C}_{\max}}$ and f_λ to total excess volume, $V(1,A\,;3)$, $n = 3$

The excess volume of a solitary wave between porosities f_0 and A is defined by

$$V(f_0,A\,;n) = 2\int_0^{\zeta(f_0)} (f-1)\,\mathrm{d}\zeta$$

$$= -2c\int_A^{f_0} \frac{(f-1)}{\mathscr{C}}\,\mathrm{d}f. \qquad (\mathrm{B}\,14)$$

For $n = 3$ $$V(f,A) = \tfrac{2}{3}[2(2A+1)(A-f)]^{\frac{1}{2}}[2A+f]. \qquad (\mathrm{B}\,15)$$

The total excess volume of a solitary wave above the background porosity is $V(1,A\,;n)$. Table 1 shows the fraction of total excess volume contained in the solitary waves for $f_0 = f_{\mathscr{C}_{\max}}$ and $f_0 = f_\lambda$ ($n = 3$). This table shows that $V(f_\lambda,A\,;3)$ contains over 90% of the excess volume for $A \gtrsim 1.5$. This result indicates that $\zeta(f_\lambda)$ is a good approximation to the half-wavelength of solitary waves.

The separation flux of melt from the matrix is $\phi(\boldsymbol{v}-\boldsymbol{V}) = k_\phi(\nabla\mathscr{C}+\boldsymbol{k})$. Substituting (B 10) gives in one dimension

$$\phi(w-W) = (1-c)+c\phi. \qquad (\mathrm{B}\,16)$$

This result can also be derived directly by integrating the definition of the compaction rate $\mathscr{C} = -(\phi(w-W))_z = -c\phi_z$. Therefore, the melt flux is $\phi w = c\phi + (1-c)$ in a frame fixed to the matrix or $fw = (1-c)$ in a frame moving with the solitary wave. This analysis is true regardless of the degree of nonlinearity n and shows that the solitary waves are the waveforms in which the melt flux becomes linear with porosity. Without the viscous compaction flux, $k_\phi \mathscr{C}_z$, the separation flux equals the forced flux and is always nonlinear in ϕ. This nonlinearity produces shocks where the melt flux decreases in the direction of flow.

Note also that in a frame moving with the waveform, the melt *velocity*, $w = (1-c)/f$ is always negative. This is the velocity at which a completely incompatible trace element would travel. Therefore porosity waves will not transport geochemical signatures indefinitely. Instead, they will pick up a signature, carry it forward and then leave it behind.

Proof: no steady solutions for step boundary conditions $n = 3$. For $n = 3$ it is straightforward to show that there are no solutions of permanent form and constant phase velocity with the boundary conditions

$$\left.\begin{aligned}
\phi(\infty) = 1, \quad & \phi(-\infty) = \phi_\mathrm{u}, \\
\mathscr{C}(\infty) = 0, \quad & \mathscr{C}(-\infty) = 0, \\
\mathscr{C}_z(\infty) = 0, \quad & \mathscr{C}_z(-\infty) = 0,
\end{aligned}\right\} \qquad (\mathrm{B}\,17)$$

when the upstream porosity $\phi_\mathrm{u} > 1$. Assuming permanent form and using only the boundary condition at ∞, the analysis is identical to that of the solitary waves up to (B 3). Equation (B 3) shows that, for $n = 3$ and fixed $c \geqslant 3$, there are only two porosities where $\mathscr{C}$ vanishes. $\mathscr{C} = 0$ at $f = 1$ and $f_0 = \tfrac{1}{2}(c-1)$. Similarly, (B 10) shows that $\mathscr{C}' = 0$ only for $f = 1$ and the single real root of $f_0^2+f_0+1 = c$. Substituting

$c = 2f_0 + 1$ in this expression shows that the only porosities where both $\mathscr{C}$ and $\mathscr{C}'$ can vanish are $f_0 = 0$ and $f_0 = 1$. This contradicts the assumption in (B 17) that $f_0 = \phi_\mathrm{u} > 1$. The proof for general n is the same but requires showing that if c is fixed, $\mathscr{C}$ and $\mathscr{C}'$ each have only one real root for $f > 1$.

REFERENCES

BARCILON, V. & LOVERA, O. 1989 Solitary waves in magma dynamics. *J. Fluid Mech.* **204**, 121–133.

BARCILON, V. & RICHTER, F. M. 1986 Non-linear waves in compacting media. *J. Fluid Mech.* **164**, 429–448.

DODD, R., EILBECK, J., GIBBON, J. & MORRIS, H. 1982 *Solitons and Non-linear Wave Equations.* Academic.

DRAZIN, P. & JOHNSON, R. 1989 *Solitons: an Introduction.* Cambridge University Press.

McKENZIE, D. 1984 The generation and compaction of partially molten rock. *J. Petrol.* **25**, 713–765.

OLSON, P. & CHRISTENSEN, U. 1986 Solitary wave propagation in a fluid conduit within a viscous matrix. *J. Geophys. Res.* **91**, 6367–6374.

PRESS, W., FLANNERY, B., TEUKOLSKY, S. & VERTTERLING, W. 1986 *Numerical Recipes.* Cambridge University Press.

RICHTER, F. M. 1986 Simple models of trace element fractionation during melt segregation. *Earth Planet. Sci. Lett.* **77**, 333–344.

RICHTER, F. M. & McKENZIE, D. 1984 Dynamical models for melt segregation from a deformable matrix. *J. Geol.* **92**, 729–740.

SCOTT, D. & STEVENSON, D. 1984 Magma solitons. *Geophys. Res. Lett.* **11**, 1161–1164.

SCOTT, D. & STEVENSON, D. 1986 Magma ascent by porous flow. *J. Geophys. Res.* **91**, 9283–9296.

SPARKS, D. W. & PARMENTIER, E. M. 1991 Melt extraction from the mantle beneath spreading centers. *Earth Planet. Sci. Lett.* **105**, 368–377.

SPIEGELMAN, M. 1989 Melting and melt migration: The physics of flow in deformable porous media. Ph.D. thesis, University of Cambridge.

SPIEGELMAN, M. 1990 Focusing on Freezing: A new mechanism for lateral melt migration at mid-ocean ridges. *EOS Trans. Am. Geophys. Union*, **71**, 1829.

SPIEGELMAN, M. 1991 2-D or not 2-D: Understanding melt migration near a sloping, freezing boundary. *EOS, Trans Am. Geophys. Union* **72**, 265.

SPIEGELMAN, M. 1993 Flow in deformable porous media. Part 1. Simple analysis. *J. Fluid Mech.* **247**, 17–38.

WHITHAM, G. 1974 *Linear and Non-linear Waves.* Wiley.